

Differentiable Microscopy Designs an All Optical Quantitative Phase Microscope

Kithmini Herath^{2,†}, Udith Haputhanthri^{1,2,†}, Ramith Hettiarachchi^{2,†}, Hasindu Kariyawasam^{2,†}
Azeem Ahmad³, Balpreet S. Ahluwalia³, Chamira U. S. Edussooriya², and Dushan Wadduwege^{1,*}

¹Center for Advanced Imaging, Faculty of Arts and Sciences, Harvard University, Cambridge, USA

²Department of Electronic and Telecommunication Engineering, University of Moratuwa, Sri Lanka

³UiT The Arctic University of Norway

*wadduwege@fas.harvard.edu

Abstract

Ever since the first microscope by Zacharias Janssen in the late 16th century, scientists have been inventing new types of microscopes for various tasks. Inventing a novel architecture demands years, if not decades, worth of scientific experience and creativity. In this work, we introduce Differentiable Microscopy ($\partial\mu$), a deep learning-based design paradigm, to aid scientists design new interpretable microscope architectures. Differentiable microscopy first models a common physics-based optical system however with trainable optical elements at key locations on the optical path. Using pre-acquired data, we then train the model end-to-end for a task of interest. The learnt design proposal can then be simplified by interpreting the learnt optical elements. As a first demonstration, based on the optical 4- f system, we present an all-optical quantitative phase microscope (QPM) design that requires no computational post-reconstruction. A follow-up literature survey suggested that the learnt architecture is similar to the generalized phase concept developed two decades ago. We then incorporate the generalized phase contrast concept to simplify the learning procedure. Furthermore, this physical optical setup is miniaturized using a diffractive deep neural network (D2NN). We outperform the existing benchmark for all-optical phase-to-intensity conversion on multiple datasets, and ours is the first demonstration of its kind on D2NNs. The proposed differentiable microscopy framework supplements the creative process of designing new optical systems and would perhaps lead to unconventional but better optical designs.

1. Introduction

Even though the invention of microscopes dates back to the late 16th century, it was during the late 19th to 20th

[†] These authors contributed equally to the work.

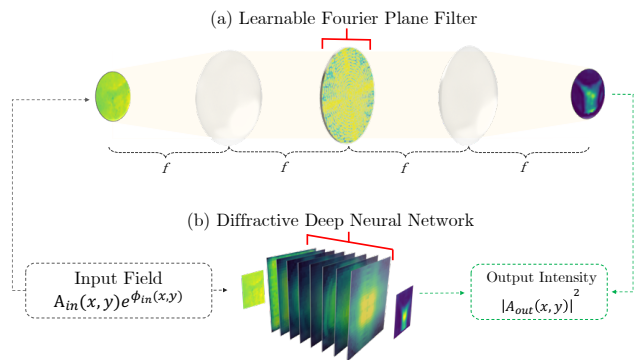


Figure 1. **Differentiable microscopy ($\partial\mu$) based all-optical phase to intensity conversion.** a) Learnable Fourier plane filter utilizing the optical 4- f system b) diffractive deep neural network. Here, f denotes the focal length of the lens used to implement the 4- f system.

century that the field saw a major renaissance [40]. This is especially due to the requirement of cross-domain scientific knowledge and creativity. For instance, as much as the knowledge of physics that is essential to build optical systems, fields such as chemistry (for sample preparation) and computer science (for image post-processing), play an important role in developing novel microscope architectures. Typical microscopy instrumentation involves understanding: the light-matter interaction at the specimen, how light propagate through optics, and how the final image is formed. The scientist's job is to design the optics such that the final image contains desired information about the measurands. This creative process may require enormous fuzzy calculations on the light propagation just to initialize a potential optical design for a new measurement task. In this work, we explore how deep learning can help ignite the creative design process for a new measurement task.

Deep learning has been increasingly used in various mi-

croscopy methods to perform tasks such as denoising, image reconstruction, and classification [29, 39, 42]. Despite the significant performance boost in such methods, the limitations inherited from the hardware of the microscope set the upper performance bound [7]. Therefore, over the past decade, researchers have focused on joint deep-learning optimization of not only the reconstruction model but also the hardware of the microscope itself [3, 5, 13, 17, 27, 36]. Nevertheless, all these methods’ focus was to optimize a system that is already capable of a specific imaging task. In contrast, we focus on the *use of machine learning to discover new optical systems* to do a new task; in other words, here our main focus is on the optical design process itself, rather than data-driven optimization of an *existing design*. To this end, we propose differentiable microscopy ($\partial\mu$), a deep learning-based design paradigm, to design new interpretable microscope architectures without requiring considerable domain knowledge.

We chose all-optical quantitative phase measurement as a first problem for $\partial\mu$. Measuring phase information of a light field is a longstanding problem in optics with valuable applications in live cell imaging [14, 23, 24, 26, 33]. Live cells are thin and transparent. They are referred to as phase objects as they mainly affect the phase of the light field. Imaging devices however only measure the intensity of light. To measure the phase, sophisticated interferometric systems are needed. This class of instruments are called quantitative phase microscopes (QPMs). QPMs interfere the phase object’s light wave (object wave) with a second known light wave (called the reference wave) resulting in interference patterns (called interferograms). Phase images are then reconstructed from interferograms, by computationally solving an inverse problem. In this work, we use differentiable microscopy to design a quantitative phase microscope (QPM) that does not require computational reconstruction. In our design the resulting interference pattern (i.e. the intensity variation at the detector) itself is the phase image (i.e. the phase variation of the object wave).

This all-optical phase to intensity conversion is a challenging design task with no general analytical solution using linear optics. Thus we first confirmed the existence of approximate solutions for given data distributions, by training a complex linear convolutional neural network (CNN) mimicking optical constraints. Second, for the same task, we trained a simple $\partial\mu$ architecture based on the optical 4- f system and a Fourier filter, as shown in Fig. 1. The selection of the architecture was driven by the fact that a lense can optically perform Fourier Transform, and hence convolutions as multiplications. No explicit knowledge about interferometry was used during the design of the architecture. Interestingly, in a followup literature survey we found a similar design called the generalized phase contrast (GPC) method introduced by Glückstad [8], through careful analytical treat-

ment of the problem. We then compared the reconstruction performance of our learned $\partial\mu$ design with the GPC design. Furthermore, we perform an analysis by starting the optimization procedure from the generalized phase contrast filter. Then, to simplify the optical 4- f setup to a much compact physical design, we train a diffractive deep neural network (D2NN) [21]. We then did an extensive performance comparison on datasets of HeLa cells, MNIST digits [18] and Bacteria, using them as phase objects. Our simulation results show that these learned all-optical designs provide better reconstruction quality than the generalized phase contrast method. Contributions of the proposed differentiable microscopy ($\partial\mu$) for all-optical QPM can be summarized as follows,

- Modelling and optimization of physics based optical systems to invent an all-optical QPM design that requires no post-processing.
- First demonstration of phase-to-intensity conversion through D2NNs.
- Comparison of the learned architectures and filters with the generalized phase contrast concept.
- Evaluation of phase-to-intensity reconstruction performance on acquired dataset of HeLa cells, MNIST and Bacteria.

2. Related Work

Image Reconstruction through Post-processing. Commonly, images acquired from microscopy techniques need processing before they can be used for desired tasks. In the context of phase imaging, deep learning has shown promise in improving microscopy techniques through the post-processing of acquired images. These methods approximate the inverse function of imaging models and have applications such as virtual staining [28, 31] and phase retrieval [32, 35].

Optical Hardware Optimization. Rather than following the static optical setup of the microscope and post-processing its acquired images, recent methods have focused on optimizing certain parts of the optical hardware itself. Several approaches focus on optimizing the illumination patterns of the microscope [5, 13, 17, 27]. This research direction of jointly optimizing the forward optics (by learning illumination patterns) with the inverse reconstruction model has been able to reduce the data requirement in QPM [15, 16]. However, since the focus is only on the *illumination aspect*, the extent to which the forward optics model can be optimized is constrained. In contrast, in differentiable microscopy ($\partial\mu$), here we focus on learning new optical systems, and interpretable design rules.

Fourier Plane Filter Optimization. The $4-f$ optical system (Fig. 1(a)) produces the Fourier transform of the incident spatial light at the Fourier plane. This Fourier transform property of a lens can be leveraged to perform the convolution operation through light itself by placing filters at the Fourier plane. The effectiveness of this optical convolution has been studied in the literature to perform various classification tasks [2, 4, 6, 41].

All-Optical Phase Retrieval Methods. The work of Zernike [44, 45] paved the way to clearly visualize transparent biological samples under a microscope without applying contrast dyes onto the specimen. Thus, the development of phase contrast microscopy is a significant milestone in biological imaging. This phase contrast method is implemented in a common-path interferometer where the signal and reference beams resulting from the illumination travel along the same optical axis and interfere at the output of the optical system generating an interferogram. The phase perturbations introduced by the optical characteristics (refractive index, thickness) of the object are converted to observable intensity variations on the interferogram, by the use of a Fourier plane filter in the optical path. This filter functions as a phase shifting filter which imparts a quarter-wave shift on the undiffracted light components (the reference beam). However, the linear relationship between the input phase and output intensity of this system is derived based on the “small-scale” phase approximation, where the largest input phase deviation is considered to be $\pi/3$. Glückstad [8] generalized Zernike’s phase contrast method and introduced the generalized phase contrast (GPC) method to provide an all-optical linear phase to intensity conversion approach, which overcomes the restriction of “small-scale” phase approximation. The descriptive mathematical analysis of the filter implementation in [9] shows the utilization of a phase shifting Fourier plane filter, where its parameters are carefully selected to appropriately generate the synthetic reference wave (SRW) to reveal the input phase perturbations in the output interference pattern. Through further mathematical analysis they have demonstrated how the system parameters can be optimized to produce accurate phase variation measurements and reduce the error in quantitative phase microscopy when a GPC-based method is utilized with post-processing. Even though the GPC method is capable of linearly mapping the input phase information to the output intensity all optically, it requires a careful mathematical analysis, a considerable amount of domain knowledge and relatively complex optical setups with post-processing to implement quantitative phase imaging. On the other hand, in our implementation the microscope is optimized for phase reconstruction as an end-to-end differentiable model.

Diffractive Deep Neural Networks. D2NNs are a type

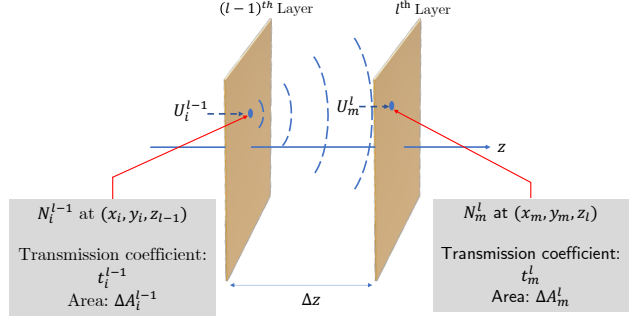


Figure 2. Diffraction of light waves by a neuron of a D2NN layer.

of optical neural networks which is introduced by Lin *et al.* [21] as a physical mechanism to perform machine learning. They consist of a set of diffractive surfaces acting as the layers of the machine learning model. The transmission coefficients of each diffractive element act as the neurons of the network and they can be trained by modelling them with optical diffraction theory. The trained diffraction surfaces can be 3D printed and inference is done by propagating light through the D2NN. Since they work purely optically, the D2NNs has the capability of performing computations at the speed of light with no power consumption. D2NNs are utilized for various tasks such as image classification [19, 20], object detection and segmentation [43], designing task-specific optical systems [22], reconstruction of overlapping phase objects [25], and image reconstruction using holograms [34]. In contrast to this, we utilize the D2NN for the direct phase to intensity conversion. Our method is the first demonstration of phase-to-intensity conversion through D2NNs to the best of our knowledge.

3. A Brief Review of Diffractive Deep Neural Networks

As previously discussed, a D2NN comprises of a set of diffractive layers. Each diffractive element (neuron) in a diffractive layer can be considered as a secondary wave source according to the Huygens-Fresnel principle [21]. The diffraction at each neuron can be modelled using the Rayleigh-Sommerfeld diffraction formulation [11] as follows.

As shown in Fig. 2, suppose that the field at the i^{th} neuron of the $(l-1)^{\text{th}}$ layer (N_i^{l-1}), which is located at (x_i, y_i, z_{l-1}) is given by U_i^{l-1} , and the diffraction caused at this neuron results in the field given by $U_{m,i}^l$ at N_m^l located at (x_m, y_m, z_l) . Then, $U_{m,i}^l$ is given by,

$$U_{m,i}^l = U_i^{l-1} t_i^{l-1} w_{m,i}^l \Delta A_i^{l-1}, \quad (1)$$

where

$$w_{m,i}^l = \left(\frac{\Delta z}{r_{m,i}^2} \right) \left(\frac{1}{2\pi r_{m,i}} + \frac{1}{j\lambda} \right) \exp \left\{ \left(\frac{j2\pi r_{m,i}}{\lambda} \right) \right\}. \quad (2)$$

Here, ΔA_i^{l-1} is the area of N_i^{l-1} , t_i^{l-1} is the transmission coefficient of the same neuron, λ is the wavelength of the optical wave, $\Delta z = z_l - z_{l-1}$ is the distance between the two adjacent layers along the direction of light propagation, $r_{m,i} = \sqrt{(x_m - x_i)^2 + (y_m - y_i)^2 + \Delta z^2}$, and $j = \sqrt{-1}$. The overall resulting field at N_m^l is the superposition of all the fields resulted by the diffraction at each of the neurons at the $(l-1)^{\text{th}}$ layer which is given by

$$U_m^l = \sum_i U_{m,i}^l. \quad (3)$$

However, direct implementation of these equations results in resource intensive computations in the simulations. A more computationally efficient modelling is done using the fact that the field resulted by an optical wave and its angular spectrum are related through the Fourier transform [11, 30]. Hence, the resulting field at the l^{th} layer (U^l) can be obtained from the field at the $(l-1)^{\text{th}}$ layer (U^{l-1}), the transmission coefficient matrix of the $(l-1)^{\text{th}}$ layer (t^{l-1}) and the propagation transfer function $G(\Delta z)$ as given by

$$U^l = IDFT2 \{ DFT2 \{ U^{l-1} \circ t^{l-1} \} \circ G(\Delta z) \} \quad (4)$$

$$G(\Delta z) = \exp \left\{ \left(j2\pi \Delta z \sqrt{\frac{1}{\lambda^2} - f_x^2 - f_y^2} \right) \right\}. \quad (5)$$

Here, \circ , $DFT2\{\cdot\}$ and $IDFT2\{\cdot\}$ represent the element-wise matrix multiplication, 2-D discrete Fourier transform (DFT), and 2-D inverse DFT operations respectively where, f_x and f_y are the spatial frequencies of the angular spectrum. Further details on the mathematical modelling of D2NNs are given in the supplementary materials.

4. Methodology

We propose all-optical end-to-end differentiable microscopy designs based on: 1) Learnable Fourier filter and 2) *PhaseD2NN*, which are capable of converting phase information to intensity through light propagation. In this section, we describe 1) The main objective: phase reconstruction loss, 2) The feasibility of linear phase retrieval by training a complex linear CNN, 3) The learnable Fourier filter for phase retrieval, and 4) *PhaseD2NN*.

4.1. Phase Reconstruction Loss

To accomplish the task of converting the phase-to-intensity, we propose *phase reconstruction loss*. The input electric field, $x_{in} = A_{in} e^{j\phi_{in}}$ is propagated through

the proposed model H to produce the output electric field $x_{out} = A_{out} e^{j\phi_{out}}$. Then the phase reconstruction loss can be defined as

$$\mathcal{L}_\phi = \mathbb{E}_{x_{in} \sim P_X} [Rh(|A_{out}|^2, \phi_{in}/(2\pi))], \quad (6)$$

where, P_X , $Rh(\cdot)$ represents the probability distribution of phase objects and the Reverse Huber Loss [46], respectively. We consider $\phi_{in} \in [0, 2\pi]$. More details regarding the choice of the loss function are discussed in supplementary materials.

4.2. Feasibility of Linear Phase Retrieval

Initially, we explore the feasibility of linear conversion of phase information to intensity by utilizing a complex-valued linear CNN. We consider it important to confirm the feasibility since there is no general analytical solution using linear optics for this challenging task of all-optical phase to intensity conversion.

We train a complex-valued CNN with the objective of reconstructing the input phase at the output intensity. The CNN consists of five convolutional layers which utilizes a single channel kernel size of three at each layer and no non-linear activations. Experimentally we observed that the network was unable to reconstruct the phase at the intensity without bias terms in the layers, therefore, we only used a bias term at the last convolutional layer instead of applying a bias term to all layers so that an analogous optical network can be easily mimicked, where this bias can be considered to be a reference wave in optics. Moreover, applying bias terms in all layers did not show an apparent improvement in results.

4.3. Learnable Fourier Filter for Phase Retrieval

The learnable Fourier filter is based on the $4-f$ system [12]. Similar to phase contrast based common path interferometric approaches found in the literature [8, 44, 45], we introduce a circular passive filter in the Fourier plane of this system. Our work distinguishes from the literature by the additional learnable capability introduced to learn the filter to *linearly convert input phase images to intensity*. We model the system as shown in Fig. 1(a) where the circular filter consists of complex-valued learnable transmission coefficients within a 128×128 grid. The circular region occupies the maximum area within the grid with the coefficients out of the circular region set to 0 (see filters in Fig. 5). The phase weights and amplitude weights of the learnable transmission coefficients are randomly initialized and a constraint of $[0, 1]$ is applied for the amplitude weights. The optical elements characterized by these transmission coefficients are compactly placed within the filter. The input field is directed to the model through a circular aperture having the same radius as the filter. However in the simulation, the information of the phase object is in a circular region within

a 32×32 grid and a $4 \times$ padding was added which makes up the 128×128 grid. Padding the input proved to improve the intensity reconstruction at the output since padding the input results in an increased number of samples in the Fourier domain, which leads to a more accurate frequency representation at the Fourier plane of the 4- f system. The first lens of the 4- f system takes the Fourier transform of this input field, which is subjected to a linear transformation by the filter in the Fourier plane and then converted back to the spatial domain by a Fourier transform of the second lens. This physical system is mathematically modeled as in the eq. (7) and the trainable complex coefficients are optimized through the loss function presented in the eq. (6).

$$H\{\cdot\} \equiv IDFT2\{H_t \circ DFT2\{\cdot\}\} \quad (7)$$

where H_t represents the learnable transmission coefficient matrix.

4.3.1 GPC-based Initialization

The GPC introduced by Glückstad [9] is a circular filter in the Fourier plane consisting of 2 main regions, namely; the central region and the outer region. In this implementation, a phase shift is introduced by the central region of the filter which results in an interference pattern that produces a substantial contrastive image of the input phase object. Therefore, with the goal of improving the performance of the existing filter, rather than randomly initializing the filter weights, we initialized the weights with the GPC filter parameters to train the network. After experimenting with different filter combinations on the datasets (Section 5.1) we selected the GPC transmission coefficients to have unit amplitude, $\pi/2$ phase shift in the central region and, 0 phase shift in the outer region.

Learned Transformation Loss.

Phase reconstruction loss (\mathcal{L}_ϕ) explained in Section 4.1 forces the intensity of the output field to match the normalized input phase image which is in the range $[0, 1]$. In contrast, the reconstructed phase of GPC does not necessarily fall within the range $[0, 1]$ [8]. Therefore we propose *Learned Transformation Loss* which gives the model the flexibility to choose the range that the reconstruction of the phase image occur, instead of forcing it to be in the range of $[0, 1]$. The proposed loss is defined as

$$\mathcal{L}_{LT} = \mathbb{E}_{x_{in} \sim P_X} \left[Rh \left(\frac{|A_{out}|^2 - B}{S}, \frac{\phi_{in}}{2\pi} \right) \right], \quad (8)$$

where B and S are learnable matrices or scalars which are optimized jointly with the end-to-end model. In our experiments we consider B to be fixed and set $B = 0$, while S is considered to be a learnable scalar.

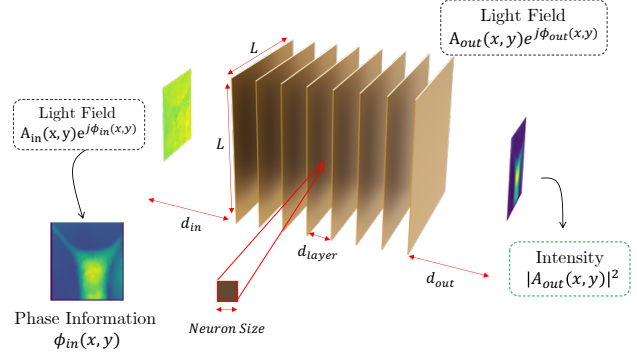


Figure 3. **PhaseD2NN Architecture:** Information of interest is in the phase of the light field (ϕ_{in}) which is not detectable by a camera. PhaseD2NN converts the phase information to intensity at the output image plane ($|A_{out}|^2$).

4.4. Phase Diffractive Deep Neural Network

In this section, we propose *Phase Diffractive Deep Neural Network (PhaseD2NN)*, an all-optical, compact, efficient framework for quantitative phase imaging. Because of the dense placement of diffractive layers, this design reduces the space and the experimental complexity of the optical 4- f system. To the best of our knowledge, this is the first demonstration of phase-to-intensity conversion using D2NNs.

The proposed architecture is shown in Fig. 3. Given the wavelength (λ) of the light waves used to illuminate the network, the network consists of 8 diffractive layers which are separated by 5.3λ distance. Each layer of the network consists of a 128×128 neuron grid that contains trainable complex-valued transmission coefficients. The size of each neuron is $\lambda/2 \times \lambda/2$ and arranged without a separation. The input to the network is a phase object, which is a complex-valued image, where the information of interest can be found in its phase. This input phase object is located in a 32×32 grid, 5.3λ before the first layer of the D2NN. The reconstruction plane or the image plane is considered to be situated with 9.3λ distance from the last optical layer. The reconstruction is done on 32×32 grid on this reconstruction plane. The element size of the input grid and reconstruction grid is same as the size of a neuron. Hence, this compact system has dimensions of $64\lambda \times 64\lambda \times 51.7\lambda$. Furthermore, layers and input phase object are aligned with the optical axis of the system.

After mathematically modelling the diffractive layers as mentioned in section 3, the learnable transmission coefficients (t_i) of each layer are optimized with the objective defined in eq. (6). To maintain the passive nature of the layers, we constrain the amplitudes of the transmission coefficients to the range $[0, 1]$.

5. Experiments and Results

We first demonstrate the datasets in section 5.1 which are used for the evaluation of the method and discuss the feasibility of linear phase retrieval in section 5.2. Then in section 5.3, the *learnable Fourier filter* is evaluated on different datasets while comparing with the existing GPC method. Furthermore, we discuss the generalizability of the learnable Fourier filters. The section 5.4 demonstrates the evaluation of the proposed *PhaseD2NN* on sparse datasets and the use of *PhaseD2NN* towards QPM. Finally, in the sections 5.5 and 5.6, we summarize the overall results of the proposed methods and discuss the limitations of our work.

5.1. Datasets

For the experiments, we have considered the following datasets.

Phase MNIST Digits. To preserve consistency with existing studies [21] we consider the *Phase MNIST digit* dataset for evaluation. To construct this dataset, we convert the images from the MNIST digit dataset to phase images ($e^{j\phi_{in}}$) such that $\phi_{in} \in [0, \pi]$. We considered this dataset as a *sparse dataset* because it contains relatively less complex structures (e.g. Contains only a single digit located at the center of the image grid)

HeLa Dataset. To evaluate the proposed method on microscopy, we acquire a dataset of *HeLa* cells where the samples are illuminated with 600 nm light.

More details regarding the sample preparation and acquisition procedure can be found in the supplementary materials. The dataset has phase information $\phi_{in} \in [0, 2\pi]$. Furthermore, to study the effect of the phase angle distribution on the reconstruction performance, we have created a scaled version of this dataset such that $\phi_{in} \in [0, \pi]$.

Bacteria Dataset. This is another acquired dataset for the purpose of evaluating the network performances for microscopy. The dataset has phase information $\phi_{in} \in [0, 2\pi]$. This can also be considered as a *sparse dataset* similar to the Phase MNIST dataset.

Phase Noise Dataset. The Phase Noise dataset is created by utilizing noise images in both phase and amplitude. This dataset is used to train a generalizable learnable Fourier filter. We induce different sparsity levels for noise when creating the datasets which are important for demonstrating the generalizability of learned Fourier filter in Section 5.3.

5.2. Feasibility of Linear Phase Retrieval

Table 1 and Fig. 4 depicts that the complex-valued CNN performs well for phase to intensity conversion tasks when the phase information is within a smaller phase range $[0, \pi]$

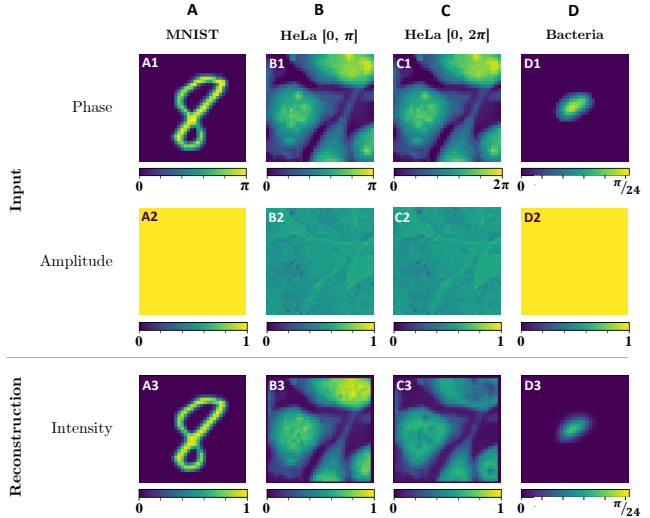


Figure 4. Complex-valued linear CNN for all-optical phase retrieval.

Dataset	Performance	
	SSIM \uparrow	L1 \downarrow
Phase MNIST $[0, \pi]$	0.9727	0.0125
HeLa $[0, \pi]$	0.9052	0.0302
HeLa $[0, 2\pi]$	0.7059	0.0635
Bacteria $[0, 2\pi]$	0.9631	0.0019

Table 1. Performance of complex-valued linear CNNs

compared to $[0, 2\pi]$.

The quantitative and qualitative results establishes the existence of linear approximate solutions for given data distributions, while also setting empirical upper bounds for the task.

5.3. Learnable Fourier Filter for Phase Retrieval

5.3.1 Learned Filter Comparison with GPC

We perform a comparison of our learned Fourier filters with the filters implemented by the GPC method as shown in Fig. 5. Considering our learned filters on the HeLa dataset in comparison to the filters from the GPC method, it is evident that the amplitudes of the transmission coefficients are unity across the circular region for the learnable Fourier filter and GPC initialized filter experiments. Furthermore, the phase coefficients of the filters have learnt a structure similar to the GPC filter which consists of a central region enabling a reference beam, and an outer region even after randomly initializing the filter coefficients during training (filters marked with blue shapes). The outer region of the learnt phase coefficients differ for the three datasets due to the different frequency content in each dataset.

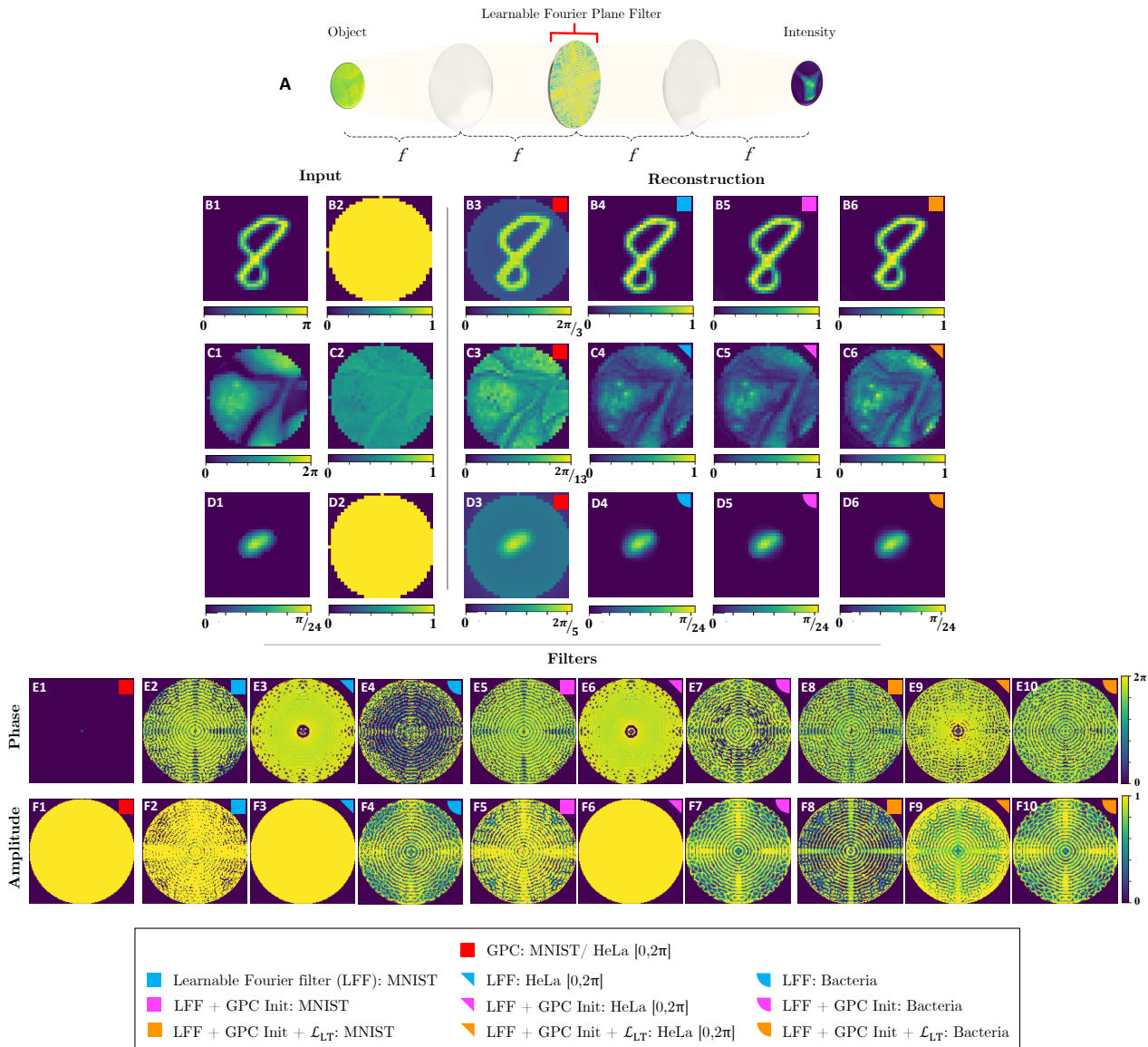


Figure 5. **Learnable Fourier filter for phase reconstruction.** A) Learnable Fourier filter placed within the 4- f system to retrieve phase information of a sample. Inputs and results of the ablation study for the learnable Fourier filter using B) Phase MNIST digit dataset, C) HeLa $[0, 2\pi]$ dataset, and D) Bacteria dataset are also shown. The corresponding learned filters are shown below them (Refer to the legend).

Furthermore, note the learnt amplitude coefficients of the filters for the second and third experiments (marked with blue and pink colored shapes). For the Phase MNIST and Bacteria datasets the amplitude coefficients have a degree of attenuation compared to that for the HeLa dataset. We interpret that this behavior is due to the sparsity of the phase objects of the three datasets. Phase MNIST and Bacteria images have large background regions with zero phase. The output intensity image should thus create this background through destructive interference. To achieve destructive in-

terference we believe the amplitude of the object and the reference arms of the filter should be carefully balanced. In our method the filter learns to attenuate each frequency band so that self-interference can generate large dark regions with destructive interference. In contrast GPC filter is incapable of generating the dark background as depicted in Fig.5-B3,D3.

However, for the experiments with \mathcal{L}_{LT} loss, the amplitude coefficients have learnt a considerable pattern for all datasets. Here the loss function relaxes reconstruction

intensity range from having to be in $[0, 1]$. This seems to enable the filter to further fine-tune to the particular dataset.

Our results clearly show that an improved reconstruction (beyond GPC) can be obtained for each dataset by appropriately learning outer region of the Fourier filter. Next, we experimented on the effect of the central region in our filters. We removed the outer regions’ patterns (on both phase and amplitude) and considered only the central regions. The modified filter still achieved 35%-64% of the original SSIM value (Sec. B.1) on the validation data. This demonstrated that the behavior introduced by the central region of the learned filters is still important and similar to the filters from the GPC method [9].

Moreover, the learned filters for a particular dataset will not essentially generalize for other datasets. To address generalization, we conducted an experiment which can learn a generalized filter for sparse and dense datasets separately (see section D.1 in the supplementary material). The results are not as impressive since a generalized linear operation for the task does not exist (in agreement with Eq. 3.14 in chapter 3 of [9]). It depicts that the mapping from phase to intensity is an approximation that depends on the data distribution.

5.3.2 Ablation Study

For a better comparison of baseline GPC method* with our method, we have selected the output intensity range that maximizes the SSIM score separately for each dataset. For the selection of this range, a separate subset of the dataset is considered.

Performance on Phase MNIST Digit Dataset. Table 2 shows the ablation study for the proposed learnable Fourier filter on Phase MNIST digit dataset. The proposed method outperforms the GPC method by a large margin of 0.48 on SSIM. Utilizing GPC-based initialization, we obtain a slight improvement in the performance. Furthermore, the adaptability of the loss function induced through \mathcal{L}_{LT} improves the performance of the proposed learnable filter with a SSIM margin of 0.03, which is an improvement of 0.5 compared to the baseline GPC method.

The qualitative results of the study are shown in Fig. 5 B. The learned phase and amplitude values of the corresponding filters are shown in the *phase* and *amplitude* rows. The GPC method (5 B3) has failed to attenuate the power of the incoming wave appropriately due to the uniform amplitude of its filter (5 filters (red)). In contrast, the learnable Fourier filter has adjusted the amplitude along with the phase of the transmission coefficients to reconstruct the background and foreground appropriately (5 filters (blue, pink, orange square shapes)). We conduct an experiment to test the generalizability of this learned Fourier filter on the FashionMNIST dataset. The obtained SSIM of 0.4665 demonstrates

Method	Performance	
	SSIM \uparrow	L1 \downarrow
MNIST: GPC*	0.4175	0.3133
MNIST: LFF	0.8933	0.0267
+ GPC init	0.8991	0.0269
+ GPC init+ \mathcal{L}_{LT}	0.9184	0.0228
- Generalizability on FashionMNIST	0.4665	0.2330
HeLa $[0, 2\pi]$: GPC*	0.3862	0.1625
HeLa $[0, 2\pi]$: LFF	0.5919	0.1133
+ GPC init	0.5921	0.1133
+ GPC init+ \mathcal{L}_{LT}	0.5719	0.1050
Bacteria $[0, 2\pi]$: GPC*	0.0528	0.1985
Bacteria $[0, 2\pi]$: LFF	0.9818	0.0009
+ GPC init	0.9816	0.0009
+ GPC init+ \mathcal{L}_{LT}	0.9820	0.0010

* Output range is selected for each dataset

Table 2. Learnable Fourier Filter (LFF): Ablation Study on Phase MNIST digit, HeLa and Bacteria datasets.

a weak generalizability towards the unseen FashionMNIST dataset, which is a dataset of similar complexity compared to the Phase MNIST digit dataset. Moreover, this behavior aligns with our discussion on generalizability in section 5.3.

Performance on the HeLa Dataset. Table 2 shows the ablation study of the proposed method on HeLa dataset. Similar to the performance on the Phase MNIST digit dataset, we show that the proposed method outperforms the GPC method with 0.2057 SSIM margin. Furthermore, utilizing GPC-based initialization slightly improves this performance. We observed that unlike the PhaseMNIST results, utilizing \mathcal{L}_{LT} degrades the performance in terms of SSIM but improves in terms of L1 distance. This may be due to the optimal convergence point of our objective function (8) is similar to the optimal convergence point of the L1 distance. Therefore it can be concluded that utilizing \mathcal{L}_{LT} still makes the convergence easier even though it results in a relatively lower SSIM.

Performance on the Bacteria Dataset. The performance of the learnable Fourier filter on the Bacteria dataset is demonstrated in Table 2. It is evident that similar to the previous experiments our learnable Fourier filter has outperformed the GPC method. Utilizing GPC-based initialization, the performance is on par with the learnable Fourier filter, suggesting that for datasets having relatively simple structures, by starting from just a random initialization, the filters can learn to obtain impressive reconstruction performance.

The qualitative results of the study are shown in Fig. 5-D

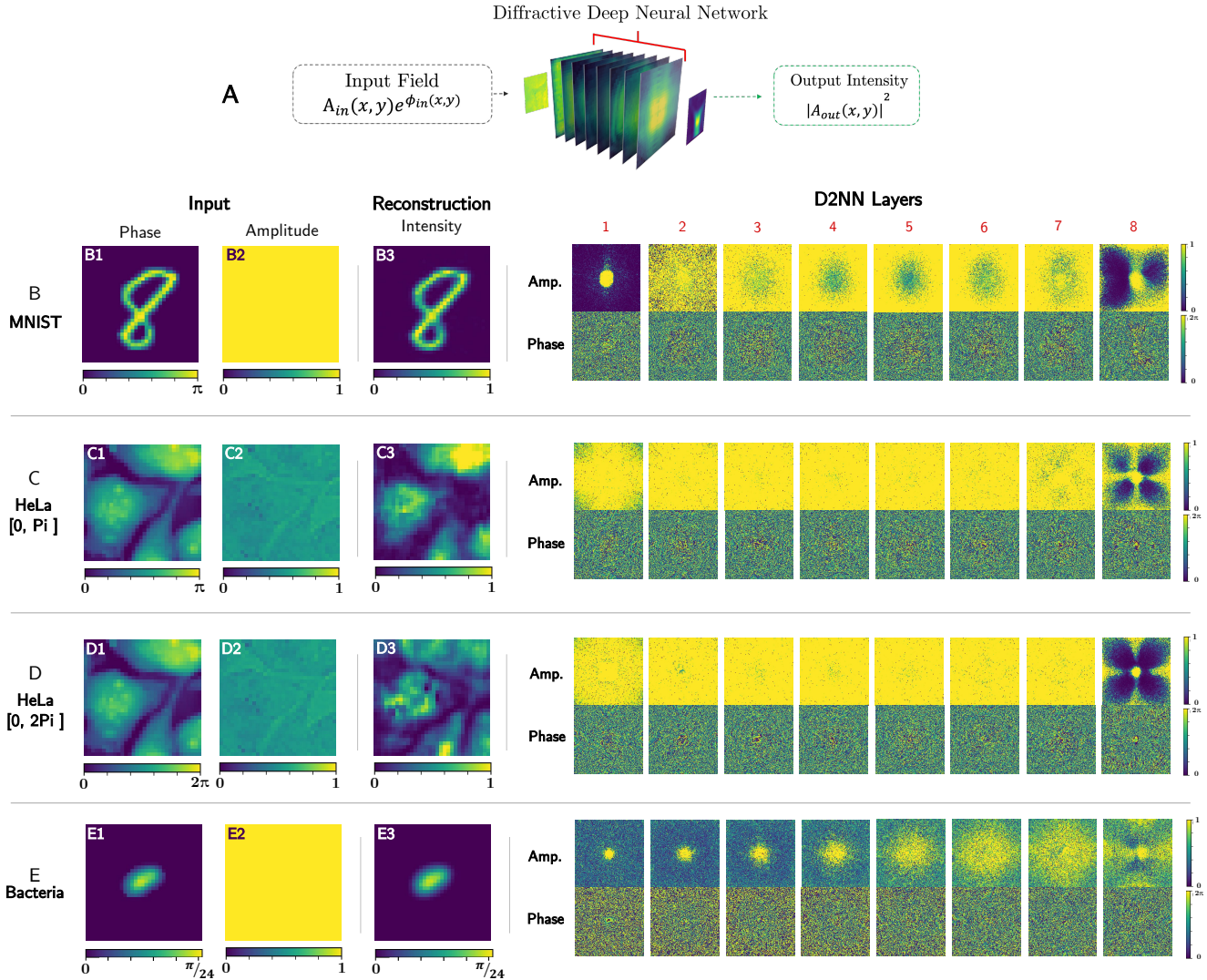


Figure 6. **PhaseD2NN for phase reconstruction.** A) PhaseD2NN with eight diffractive layers which is trained in the study. Inputs, results, learned layers are shown for B) PhaseMNIST digit dataset, C) HeLa $[0, \pi]$ dataset, D) HeLa $[0, 2\pi]$ dataset, and E) Bacteria $[0, 2\pi]$ dataset.

row. The learned phase and amplitude values of the corresponding filters are shown in the *phase* and *amplitude* rows. Considering the quantitative results in Table 2 and qualitative results in Fig. 5-D3, the GPC method has significantly failed in reconstructing the phase content appropriately due to the uniform amplitude of its filter (Fig. 5-F1). This behavior is consistent with the results obtained for the Phase MNIST dataset which is also a sparse dataset. However, the result has worsened for the bacteria dataset because the phase-shift applied only on the central region of the filter is not sufficient to cause a destructive interference at the output corresponding to the background region, which is more sparse compared to the Phase MNIST dataset.

In summary, the presented results shows the capability of our method in leveraging the properties of GPC-based filters

to learn better filter representations for the task at hand. The introduced \mathcal{L}_{LT} loss further supplements this performance when reconstructing to a specific intensity range.

5.4. Phase Diffractive Deep Neural Networks

We perform experiments using sparse datasets and move towards utilizing PhaseD2NN for quantitative phase microscopy.

Evaluation on Sparse Datasets. Table 3 shows the evaluation performances of PhaseD2NN on the Phase MNIST digit dataset. The PhaseD2NN has an SSIM score of 0.9146, which is a significant improvement of 0.50 compared to the GPC method. The qualitative results are shown in Fig. 6. The PhaseD2NN trained on MNIST dataset still

Method	Performance	
	SSIM \uparrow	L1 \downarrow
MNIST: PhaseD2NN	0.9146	0.0253
Generalizability on FashionMNIST	0.5492	0.1148
HeLa $[0, \pi]$: PhaseD2NN	0.6254	0.1059
HeLa $[0, 2\pi]$: PhaseD2NN	0.4654	0.1237
Bacteria $[0, 2\pi]$: PhaseD2NN	0.9915	0.0007

Table 3. PhaseD2NN reconstruction performance on different datasets.

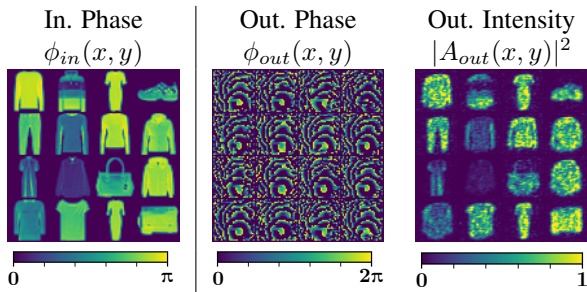


Figure 7. Evaluation of PhaseD2NN on FashionMNIST dataset after training on the MNIST dataset.

achieves an SSIM score of 0.5492 for the unseen FashionMNIST dataset. This demonstrates the generalizability of the PhaseD2NN across datasets with similar complexity. The qualitative results are shown in Fig. 7.

PhaseD2NN for Microscopy. Table 3 shows the performance of PhaseD2NN which is evaluated on two variants of the HeLa cell dataset and the bacteria dataset. It is observed that the PhaseD2NN performs well on the HeLa dataset variant which has phase information restricted to $[0, \pi]$ than the dataset which has phase information within $[0, 2\pi]$. This demonstrates that the learned PhaseD2NN performs better on phase objects with limited phase extent. Furthermore, the PhaseD2NN has achieved significant reconstruction performance on the bacteria dataset (SSIM= 0.9915). Therefore, the PhaseD2NN has been most effective on datasets of sparse nature.

5.5. Overall Comparison

Fig. 8 summarizes the best reconstruction performances achieved by the GPC, learnable Fourier filter and the PhaseD2NN on different datasets in comparison to the empirical upperbounds set by the complex-valued CNN. As noted before, the best performing output intensity region of the GPC method is selected for each dataset to achieve better SSIM results to compare with our methods.

On all three datasets, the learnable Fourier filter and the PhaseD2NN outperform the GPC method for the all-optical phase-to-intensity conversion task. Furthermore, the learnable Fourier filter achieves comparable performance to the PhaseD2NN. This result suggests that a single diffractive layer can perform on par with a diffractive deep neural network(D2NN). This is due to the fact that though comprised of many layers a D2NN is a cascade of linear operators that collapses to a single linear operation. The cascading is needed in the spatial domain to connect all pixels; but the same can be achieved by the Fourier operator. On the other hand, in comparison with the complex-valued CNN, results demonstrate that the all-optical methods can accommodate further modifications to surpass the current upper bounds for the phase-to-intensity conversion task for Phase MNIST and the two HeLa datasets. However, considering the results of the learnable Fourier filter and PhaseD2NN on the bacteria dataset, it is observed that the obtained empirical upper bound through the complex-valued CNN could be improved.

It is evident that our proposed methods perform better even for rather dense datasets, when the phase objects have phase information within a smaller range such as $[0, \pi]$. Considering the fact that these are thin phase objects where the specimen are submerged in water, the maximum phase shift would not usually exceed π . This can be mathematically shown as well for a visible wavelength of 633 nm (λ), considering a typical thickness h of a biological cell about $10\mu\text{m}$ and a refractive index difference of 0.03 with respect to a medium, the resultant phase shift would be $\phi = [2\pi(\Delta n)h]/\lambda = \pi$ rad [37]. Considering the high SSIM and low L1 error obtained from our proposed methods for the datasets having phase information within $[0, \pi]$ range, it demonstrates that our differentiable microscopy technique is capable of designing all-optical quantitative microscopes to operate within a sufficient range for quantitative phase imaging.

Considering the presented results, it is evident that utilizing deep learning and D2NN for phase retrieval and quantitative phase imaging is a promising research direction.

5.6. Limitations and Future Work

In our study, the dataset size of HeLa cells is approximately 6 times smaller than the MNIST dataset. Therefore, future work could explore to minimize the performance gap between the MNIST and HeLa cells dataset with more training data.

Moreover, the reconstruction quality of the HeLa dataset is relatively low since the reconstruction of high frequency information is challenging. However, this does not necessarily mean that it is not quantitative as we clearly reasoned it in section 5.5. We hope to analyze the optical behavior and improve the reconstruction of high frequency content

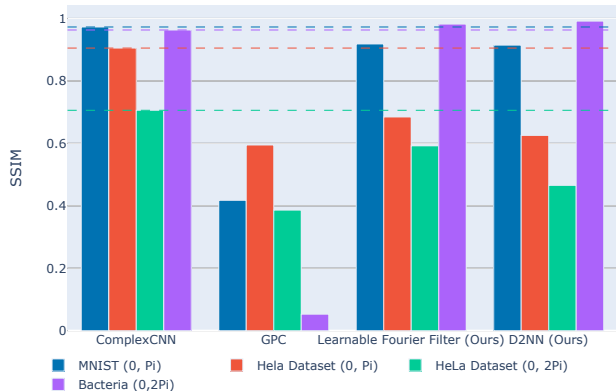


Figure 8. **Comparison of $\partial\mu$ architectures on different datasets.** Our approach significantly outperforms the GPC [9] for all three datasets. The dotted lines indicate the empirical upper bounds set by the complex-valued CNN for each dataset.

as part of our future work.

Currently, both our all optical methods are linear. Thus D2NN’s multiple layer architecture is of limited use. An important future direction is to build non-linear D2NNs that can harness the true power of cascaded diffractive layers.

Finally, while we have focused on an all-optical system in this work, we believe that the phase-to-intensity reconstruction quality can be further improved by cascading optics with electronic hardware while keeping a fine balance of the computational workload between them.

6. Conclusion

In our work, we demonstrated differentiable microscopy ($\partial\mu$), an end-to-end learning paradigm for designing microscopes by modelling an optical system and optimizing it for the task at hand. By utilizing this paradigm for all-optical phase retrieval, we proposed 1) *learnable Fourier filter microscope* and 2) *PhaseD2NN microscope*, which incorporate optical 4-*f* system and D2NNs respectively for passive phase retrieval.

Both proposed methods outperformed the GPC with a large margin for MNIST and HeLa datasets. Furthermore, the performance of the proposed PhaseD2NN is on par with the learnable Fourier filter method suggesting that, through PhaseD2NN a classical 4-*f* system based architecture could be transformed to much simpler and compact optical designs. To the best of our knowledge, this is the first demonstration of *all-optical* phase-to-intensity conversion through D2NNs. This demonstration of all-optical phase to intensity conversion will be valuable in high-throughput microscopy, two-photon polymerization based nano-fabrication [9] and optogenetics [10].

References

- [1] Azeem Ahmad, Vishesh Dubey, Nikhil Jayakumar, Anowarul Habib, Ankit Butola, Mona Nystad, Ganesh Acharya, Purusotam Basnet, Dalip Singh Mehta, and Balpreet Singh Ahluwalia. High-throughput spatial sensitive quantitative phase microscopy using low spatial and high temporal coherent illumination. *Scientific Reports*, 11(1):15850, 2021. 6
- [2] Carlos Mauricio Villegas Burgos, Tianqi Yang, Yuhao Zhu, and A. Nickolas Vamivakas. Design framework for meta-surface optics-based convolutional neural networks. *Applied Optics*, 60(15):4356, 2021. 3
- [3] Ayan Chakrabarti. Learning sensor multiplexing design through back-propagation. *Advances in Neural Information Processing Systems*, (Nips):3089–3097, 2016. 2
- [4] Julie Chang, Vincent Sitzmann, Xiong Dun, Wolfgang Heidrich, and Gordon Wetzstein. Hybrid optical-electronic convolutional neural networks with optimized diffractive optics for image classification. *Scientific Reports*, 8(1):1–10, 2018. 3
- [5] Amey Chaware, Colin L. Cooke, Kanghyun Kim, and Roarke Horstmeyer. Towards an intelligent microscope: Adaptively learned illumination for optimal sample classification. *ICASSP, IEEE International Conference on Acoustics, Speech and Signal Processing - Proceedings*, 2020-May:9284–9288, 2020. 2
- [6] Shane Colburn, Yi Chu, Eli Shilzerman, and Arka Majumdar. Optical frontend for a convolutional neural network. *Applied Optics*, 58(12):3179, 4 2019. 3
- [7] Colin L. Cooke, Fanjie Kong, Amey Chaware, Kevin C. Zhou, Kanghyun Kim, Rong Xu, D. Michael Ando, Samuel J. Yang, Pavan Chandra Konda, and Roarke Horstmeyer. Physics-enhanced machine learning for virtual fluorescence microscopy. In *Proceedings of the IEEE/CVF International Conference on Computer Vision (ICCV)*, pages 3803–3813, 2021. 2
- [8] Jesper Glückstad. Phase contrast image synthesis. *Optics Communications*, 130(4-6):225–230, 1996. 2, 3, 4, 5
- [9] Jesper Glückstad and Darwin Palima. Generalized phase contrast. *Springer Series in Optical Sciences*, 146:7–12, 2009. 3, 5, 8, 11, 4
- [10] Jesper Glückstad, RenéL. Eriksen, and Andreas Gejl Madsen. GPC-modalities for neurophotonics and optogenetics. *International Society for Optics and Photonics, SPIE*, 2021. 11
- [11] J.W. Goodman. *Introduction to Fourier Optics*. Electrical Engineering Series. McGraw-Hill, 1996. 3, 4, 2
- [12] Joseph W. Goodman and Mary E. Cox. Introduction to Fourier Optics. *Physics Today*, 22(4):97–101, 4 1969. 4
- [13] Roarke Horstmeyer, Richard Y. Chen, Barbara Kappes, and Benjamin Judkewitz. Convolutional neural networks that teach microscopes how to image. 2017. 2
- [14] Chenfei Hu and Gabriel Popescu. Quantitative phase imaging (QPI) in neuroscience. *IEEE Journal of Selected Topics in Quantum Electronics*, 25(1):1–9, 2019. 2
- [15] Michael Kellman, Emrah Bostan, Michael Chen, and Laura Waller. Data-Driven Design for Fourier Ptychographic Mi-

- croscopy. *2019 IEEE International Conference on Computational Photography, ICCP 2019*, pages 2–9, 2019. 2
- [16] Michael R. Kellman, Emrah Bostan, Nicole A. Repina, and Laura Waller. Physics-Based Learned Design: Optimized Coded-Illumination for Quantitative Phase Imaging. *IEEE Transactions on Computational Imaging*, 5(3), 2019. 2
- [17] Kanghyun Kim, Pavan Chandra Konda, Colin L. Cooke, Ron Appel, and Roarke Horstmeyer. Multi-element microscope optimization by a learned sensing network with composite physical layers. *Optics Letters*, 45(20):5684, 2020. 2
- [18] Yann LeCun, Léon Bottou, Yoshua Bengio, and Patrick Haffner. Gradient-based learning applied to document recognition. *Proceedings of the IEEE*, 86(11), 1998. 2
- [19] Jingxi Li, Deniz Mengu, Yi Luo, Yair Rivenson, and Aydogan Ozcan. Class-specific differential detection in diffractive optical neural networks improves inference accuracy. *Advanced Photonics*, 1(04), 2019. 3
- [20] Linmei Li, Shiqiang Yan, Bingcheng Lin, Qihui Shi, and Yao Lu. *Single-Cell Proteomics for Cancer Immunotherapy*, volume 139. Elsevier Inc., 1 edition, 2018. 3
- [21] Xing Lin, Yair Rivenson, Nezh T. Yardimci, Muhammed Veli, Yi Luo, Mona Jarrahi, and Aydogan Ozcan. All-optical machine learning using diffractive deep neural networks. *Science*, 361(6406), 2018. 2, 3, 6
- [22] Yi Luo, Deniz Mengu, Nezh T. Yardimci, Yair Rivenson, Muhammed Veli, Mona Jarrahi, and Aydogan Ozcan. Design of task-specific optical systems using broadband diffractive neural networks. *Light: Science and Applications*, 8(1):1–14, 2019. 3
- [23] Hassaan Majeed, Shamira Sridharan, Mustafa Mir, Lihong Ma, Eunjung Min, Woonggyu Jung, and Gabriel Popescu. Quantitative phase imaging for medical diagnosis. *Journal of Biophotonics*, 10(2):177–205, 2017. 2
- [24] Pierre Marquet, Christian Depeursinge, and Pierre J. Magistretti. Review of quantitative phase-digital holographic microscopy: promising novel imaging technique to resolve neuronal network activity and identify cellular biomarkers of psychiatric disorders. *Neurophotonics*, 1(2), 2014. 2
- [25] Deniz Mengu, Muhammed Veli, Yair Rivenson, and Aydogan Ozcan. Classification and reconstruction of spatially overlapping phase images using diffractive optical networks. pages 1–30, 8 2021. 3, 5
- [26] Mustafa Mir, Huafeng Ding, Zhuo Wang, Jason Reedy, Krishnarao Tangella, and Gabriel Popescu. Blood screening using diffraction phase cytometry. *Journal of Biomedical Optics*, 15(2), 2010. 2
- [27] Alex Muthumbi, Amey Chaware, Kanghyun Kim, Kevin C. Zhou, Pavan Chandra Konda, Richard Chen, Benjamin Judkewitz, Andreas Erdmann, Barbara Kappes, and Roarke Horstmeyer. Learned sensing: jointly optimized microscope hardware for accurate image classification. *Biomedical Optics Express*, 10(12):6351, 2019. 2
- [28] Yoav N. Nychate, Mattan Levi, Simcha K. Mirsky, Nir A. Turko, Moran Rubinfeld, Itay Barnea, Gili Dardikman-Yoffe, Miki Haifler, Alon Shalev, and Natan T. Shaked. Holographic virtual staining of individual biological cells. *Proceedings of the National Academy of Sciences of the United States of America*, 117(17), 2020. 2
- [29] Jongchan Park, David J. Brady, Guoan Zheng, Lei Tian, and Liang Gao. Review of bio-optical imaging systems with a high space-bandwidth product. *Advanced Photonics*, 3(04):1–18, 2021. 2
- [30] J. A. Ratcliffe. Some Aspects of Diffraction Theory and their Application to the Ionosphere. *Reports on Progress in Physics*, 19(1):306, 1 1956. 4, 2, 3
- [31] Yair Rivenson, Tairan Liu, Zhensong Wei, Yibo Zhang, Kevin de Haan, and Aydogan Ozcan. PhaseStain: the digital staining of label-free quantitative phase microscopy images using deep learning. *Light: Science and Applications*, 8(1), 2019. 2
- [32] Yair Rivenson, Yibo Zhang, Harun Günaydin, Da Teng, and Aydogan Ozcan. Phase recovery and holographic image reconstruction using deep learning in neural networks. *Light: Science and Applications*, 7(2), 2018. 2
- [33] Darina Roitshtain, Lauren Wolbromsky, Evgeny Bal, Hayit Greenspan, Lisa L. Satterwhite, and Natan T. Shaked. Quantitative phase microscopy spatial signatures of cancer cells. *Cytometry Part A*, 91(5):482–493, 2017. 2
- [34] Md Sadman Sakib Rahman and Aydogan Ozcan. Computer-Free, All-Optical Reconstruction of Holograms Using Diffractive Networks. *ACS Photonics*, page acsphotonics.1c01365, 10 2021. 3
- [35] Ayan Sinha, Justin Lee, Shuai Li, and George Barbastathis. Lensless computational imaging through deep learning. *Optica*, 4(9), 2017. 2
- [36] He Sun, Adrian V. Dalca, and Katherine L. Bouman. Learning a probabilistic strategy for computational imaging sensor selection. *IEEE International Conference on Computational Photography, ICCP 2020*, 2020. 2
- [37] Yongjin Sung, Wonshik Choi, Christopher Fang-Yen, Kamran Badizadegan, Ramachandra R. Dasari, and Michael S. Feld. Optical diffraction tomography for high resolution live cell imaging. *Optics InfoBase Conference Papers*, 17(1):1977–1979, 2009. 10
- [38] J. Vargas, J. Antonio Quiroga, and T. Belenguer. Phase-shifting interferometry based on principal component analysis. *Opt. Lett.*, 36(8):1326–1328, Apr 2011. 6
- [39] Hongda Wang, Yair Rivenson, Yiyin Jin, Zhensong Wei, Ronald Gao, Harun Günaydin, Laurent A. Bentolila, Comert Kural, and Aydogan Ozcan. Deep learning enables cross-modality super-resolution in fluorescence microscopy. *Nature Methods*, 16(1), 2019. 2
- [40] John P. Wourms. Light Microscopy: Renaissance and Revolution. *BioScience*, 40(5):397–399, 5 1990. 1
- [41] Qiu hao Wu, Xiubao Sui, Yuhang Fei, Chen Xu, Jia Liu, Guohua Gu, and Qian Chen. Multi-layer optical Fourier neural network based on the convolution theorem. *AIP Advances*, 11(5):1–6, 2021. 3
- [42] Yujia Xue, Shiyi Cheng, Yunzhe Li, and Lei Tian. Reliable deep-learning-based phase imaging with uncertainty quantification. 2019. 2
- [43] Tao Yan, Jiamin Wu, Tiankuang Zhou, Hao Xie, Feng Xu, Jingtao Fan, Lu Fang, Xing Lin, and Qionghai Dai. Fourier-space Diffractive Deep Neural Network. *Physical Review Letters*, 123(2), 2019. 3

- [44] F. Zernike. Phase contrast, a new method for the microscopic observation of transparent objects. *Physica*, 9(7), 1942. 3, 4
- [45] F. Zernike. Phase contrast, a new method for the microscopic observation of transparent objects part II. *Physica*, 9(10), 1942. 3, 4
- [46] Laurent Zwald and Sophie Lambert-Lacroix. The BerHu penalty and the grouped effect. 2012. 4, 5

Differentiable Microscopy Designs an All Optical Quantitative Phase Microscope

Supplementary Material

A. Mathematical Modelling of Optical Systems

A.1. 4- f system

Fig. S1 shows the system which is generally referred to as 4- f filtering architecture [11]. It is referred as 4- f because of the distance between the input plane (P_1) and the image plane (P_3) equals to $4 \times f$, where f is the focal length of the lenses. Here S is the point source, P_1, P_2, P_3 are the input plane, Fourier plane and the image plane, respectively, and L_1, L_2, L_3 are identical lenses each having a focal length f . The light from S is collimated with the lens L_1 . The input sample (P_1) which has $g(x_1, y_1)$ amplitude transmission coefficient is placed against L_1 to reduce the overall length of the system. The resultant light is then collimated with the Fourier transforming lens L_2 resulting $k_1 G\left(\frac{x_2}{\lambda f}, \frac{y_2}{\lambda f}\right)$ field at P_2 plane where G is the Fourier transform of g and k_1 is a constant. To manipulate the spectrum of input field $g(x_1, y_1)$, filter can be placed in the Fourier plane in P_2 . The transmission coefficient of the filter is given by

$$t_A(x_2, y_2) = k_2 H\left(\frac{x_2}{\lambda f}, \frac{y_2}{\lambda f}\right), \quad (1)$$

if the desired frequency domain transfer function is H and k_2 is a constant. Following lens L_3 applies the Fourier transform again on the modified spectrum to obtain the inverted modified field.

A.2. Mathematical Modelling of D2NNs

The resulting field due to the diffraction of light at each neuron in a D2NN can be modelled using the Rayleigh-Sommerfeld diffraction theory [11, ch. 3.5]. It describes the diffraction of light by an aperture in an infinite opaque planar screen. Consider such an aperture illuminated by a light wave which has a field $U(P_1)$ at a point $P_1 \equiv (x_1, y_1, z_1)$ on the aperture surface S as shown in Fig. S2.

The field at point $P_0 \equiv (x_0, y_0, z_0)$ after the diffraction can be given using the first Rayleigh-Sommerfeld solution to the diffraction problem, which is given

$$U(P_0) = \iint_S U(P_1) \left(\frac{z_0 - z_1}{r^2}\right) \left(\frac{1}{2\pi r} + \frac{1}{j\lambda}\right) e^{j\frac{2\pi r}{\lambda}} dS. \quad (2)$$

Here, $r = \sqrt{(x_0 - x_1)^2 + (y_0 - y_1)^2 + (z_0 - z_1)^2}$ is the distance between the points P_1 and P_0 , λ is the wavelength of the light wave and $j = \sqrt{-1}$. This integral holds under the conditions that, U is a homogeneous scalar wave equation and it satisfies the *Sommerfeld radiation condition*

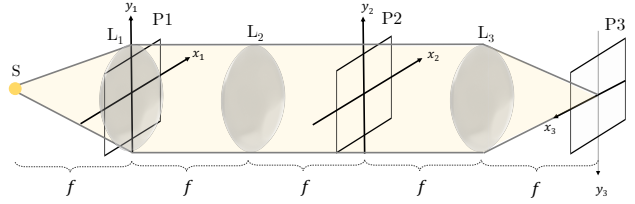


Figure S1. 4- f system

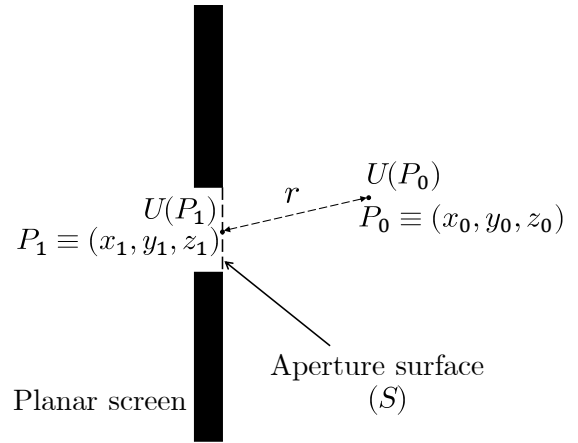


Figure S2. Diffraction by an aperture in a planar screen.

which states that U must vanish at least as fast as a diverging spherical wave [11, ch. 3.4].

This integral can be directly converted to a Riemann summation considering a discrete set of sampling points on the aperture plane. In this direct implementation, each neuron in a diffractive layer is considered as a sampling point as described in the main text. However, this results in a computationally expensive and a memory intensive modelling of the D2NN. A more computationally efficient method is used in our work to model the D2NNs known as the angular spectrum (AS) method.

A.2.1 Angular Spectrum

A plane wave can be considered as a combination of a set of plane waves travelling in different directions. The complex amplitudes of these plane wave components form the angular spectrum of the given wave [30]. Consider the field of a light wave propagating in the z direction is given by,

$$U(x, y, z, t) = U(x, y, z)e^{-j2\pi ft}, \quad (3)$$

where f is the temporal frequency of the wave. Suppose that, at $z = 0$ plane, $U(x, y, z)|_{z=0} \equiv U(0)$. It can be shown that the field $U(0)$ and its angular spectrum $A(f_x, f_y, 0) \equiv A(0)$ are related by [30],

$$U(0) = \int_{-\infty}^{\infty} \int_{-\infty}^{\infty} A(0) e^{j2\pi(f_x x + f_y y)} df_x df_y. \quad (4)$$

Here, $f_x = \frac{\alpha}{\lambda}$ and $f_y = \frac{\beta}{\lambda}$, where α and β are direction cosines of the plane wave components with respect to the x and y axes. Note that eq. (4) is of the form of 2-D inverse Fourier transform. Hence, the field and its angular spectrum can be considered as a Fourier transform pair. A generalized form of this result can be written as

$$U(z) \xleftrightarrow{\mathcal{F}} A(z), \quad (5)$$

where $U(z) \equiv U(x, y, z)$ is the field on $z = z$ plane and $A(z) \equiv A(f_x, f_y, z)$ is its angular spectrum. Suppose that the relationship between the angular spectrum at $z = 0$ and $z = z$ planes is given as

$$A(z) = A(0) G(z) \quad (6)$$

where, $G(z) \equiv G(f_x, f_y, z)$ is the propagation transfer function which characterises the propagation of the angular spectrum.

Electromagnetic waves satisfy the Helmholtz equation and therefore $U(z)$ should also satisfy it. This can be used to find an expression for $G(z)$. The Helmholtz equation is given as

$$(\nabla^2 + k^2) U(z) = 0, \quad (7)$$

where $k = \frac{2\pi}{\lambda}$ is the wavenumber which is the magnitude of the propagation vectors $\vec{k} = [k_x, k_y, k_z]$ of the wave components. Considering eq. (5), eq. (6), and eq. (7), it can be observed that $G(z)$ satisfies

$$\frac{d^2 G(z)}{dz^2} + k_z^2 G(z) = 0, \quad (8)$$

where

$$k_z = 2\pi \sqrt{\frac{1}{\lambda^2} - f_x^2 - f_y^2}. \quad (9)$$

An elementary solution to eq. (8) can be written as,

$$G(z) = e^{j2\pi z \sqrt{\frac{1}{\lambda^2} - f_x^2 - f_y^2}}. \quad (10)$$

Hence, eq. (6) can be re-written as

$$A(z) = A(0) e^{j2\pi z \sqrt{\frac{1}{\lambda^2} - f_x^2 - f_y^2}}. \quad (11)$$

This equation shows that when $f_x^2 + f_y^2 \leq \frac{1}{\lambda^2}$, the propagation of the angular spectrum along the z axis introduce

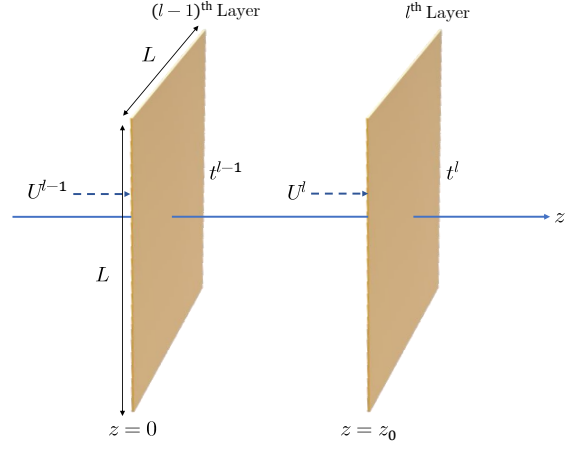


Figure S3. **Two adjacent layers of the D2NN.** The field incident on the $(l-1)^{\text{th}}$ layer is U^{l-1} which is subjected to diffraction at the layer and results the field U^l just before the next layer.

a different set of phase shift to each of the components of the angular spectrum [11]. However, when $f_x^2 + f_y^2 > \frac{1}{\lambda^2}$, eq. (11) can be written as,

$$A(z) = A(0) e^{-2\pi z \sqrt{f_x^2 + f_y^2 - \frac{1}{\lambda^2}}}. \quad (12)$$

In this case, the angular spectrum is exponentially attenuated along the z axis. These wave components are known as *evanescent waves* and they do not propagate energy along the z axis.

A.2.2 Implementation of the Angular Spectrum Method

The Fourier relationship between the electric/magnetic field of a light wave and its AS can be obtained using the discrete Fourier transform (DFT) which can be computed efficiently using a fast Fourier transform (FFT) algorithm. Consider two layers of a D2NN at $z = 0$ plane ($(l-1)^{\text{th}}$ layer) and at $z = z_0$ plane (l^{th} layer) as shown in Fig. S3. The input field at the $(l-1)^{\text{th}}$ layer is given by $U(x, y, 0) \equiv U^{l-1}$ and the resulting field at the observation plane is given by $U(x, y, z_0) \equiv U^l$. The width and the height of both layers are L where t^{l-1} and t^l are the complex transmission coefficient matrices of the two layers.

Fig. S4 shows the computation pipeline of the output field using the AS method. Initially, the input field is sampled with a sampling interval of dx in the spatial domain. The sampled input has a size of $N \times N$ samples, where $N = L/dx$. The sampled input is then multiplied element-wise with t^{l-1} to obtain the effective field at the $(l-1)^{\text{th}}$ layer which is given by

$$U_{\text{eff}}^{(l-1)} = U^{l-1} \circ t^{l-1}, \quad (13)$$

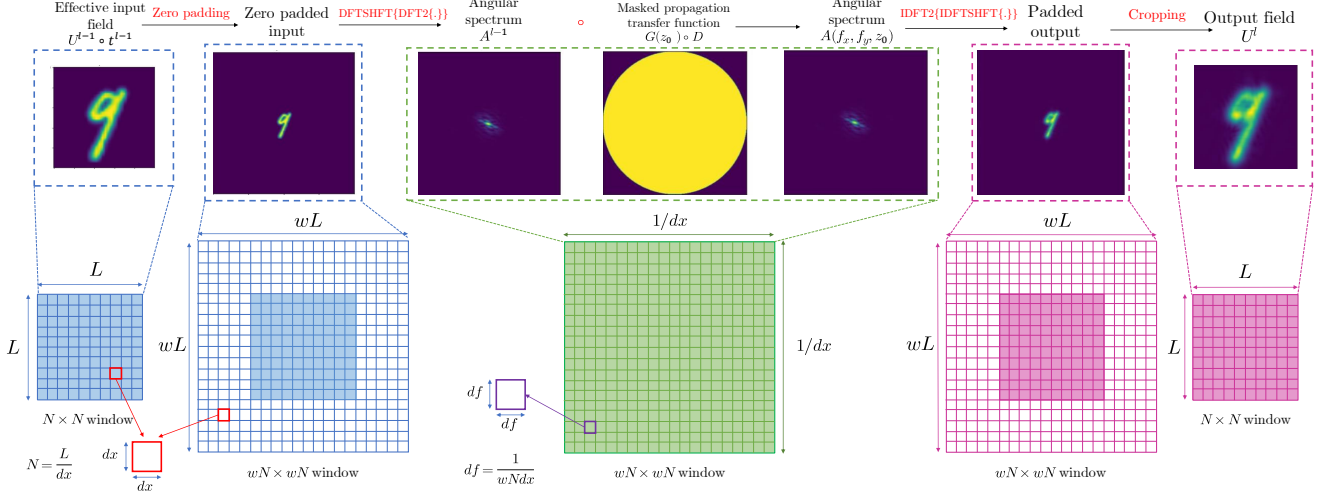


Figure S4. **Computational pipeline of the AS method.** In the figure $DFT2\{\cdot\}$ denotes the 2D-DFT operation, $DFTSHFT\{\cdot\}$ denotes the DFT shift operation, $IDFT2\{\cdot\}$ denotes the 2D-IDFT operation, $IDFTSHFT\{\cdot\}$ denotes the IDFT shift operation, and \circ denotes the element-wise matrix multiplication.

where \circ is the element-wise matrix multiplication.

Since the region of support of the input is bounded in the spatial domain, the region of support of its Fourier transform is unbounded and to get a more accurate AS, a higher number of samples of the Fourier transform need to be considered. Therefore, for the computation purposes a separate computational window of the size $wN \times wN$ samples is considered where w is the computation window factor. The oversampling in the Fourier domain is performed by zero padding U_{eff}^{l-1} at the boundary to match the size of the computation window. Then the 2D-DFT of the input field is taken followed by a DFT shift operation to make the center of the computation window $(0, 0)$ resulting the AS given by A^{l-1} .

A^{l-1} has spatial frequency components in the range of $\left[-\frac{f_s}{2}, \frac{f_s}{2}\right]$ in both f_x and f_y axes where $f_s = 1/dx$ is the sampling frequency in the spatial domain. Note that the gap between two samples in the angular spectrum is $f_s = 1/wNdx$. The propagation transfer function at $z = z_0$ $G(z_0)$ is also created in the computation window with a similar number of samples as A^{l-1} . Since the evanescent waves do not propagate energy along the z -axis, they are filtered out using a mask D . The masked propagation transfer function is given by

$$G(z_0) \circ D = \begin{cases} e^{j2\pi z_0 \sqrt{\frac{1}{\lambda^2} - f_x^2 - f_y^2}} & f_x^2 + f_y^2 \leq \frac{1}{\lambda} \\ 0 & f_x^2 + f_y^2 > \frac{1}{\lambda} \end{cases} \quad (14)$$

According to eq. (6), the AS of the field at $z = z_0$ is obtained by the element-wise multiplication of A^{l-1} and the masked propagation transfer function. Then an inverse

DFT (IDFT) shift operation is performed followed by a 2D-IDFT operation to get the padded resulting field. Finally, the padding is removed to retrieve the resulting field U^l .

B. Method

B.1. Effect of the Central Region of the Learned Fourier Filter

The goal of this experiment is to analyze the effect of the central region of the learned Fourier filter. In this experiment we obtained the learned filter and modified its weights to consider a combination of only the central region, only the outer region, full filter region of the phase weights (retaining the learned phase weights of the filter), with amplitude weights set to unity and retaining the learned amplitude weights. The considered central region was calculated according to the standard method described in Chapter 3. in [9]. The results of the experiments are summarized in Table S4.

Table S4 depicts how the modified filters for each experiment have been able to capture approximately 35% - 64% of the original SSIM by only considering the learned phase weights in the central region with unit amplitude in the entire filter region. It shows the importance of the central region of the learned filters similar to the theoretical implementation of the GPC filter. The slight improvement in SSIM when considering the learned amplitude weights instead of the unit amplitude for the Phase MNIST scenario signifies the importance of the learned amplitude weights (introduced attenuation) in addition to the phase weights in the central region. The importance in attenuating the incoming power appropriately for the reconstruction is demon-

Method	SSIM
MNIST $[0, \pi]$:	
<i>Learnable Fourier Filter</i>	0.8933
Phase (central) + unit amplitude	0.3132
Phase (central) + learned amplitude	0.3945
HeLa $[0, 2\pi]$:	
<i>Learnable Fourier Filter</i>	0.5919
Phase (central) + unit amplitude	0.3748
Phase (central) + learned amplitude	0.3748

Table S4. **Effect of the central region of the learned Fourier filter for reconstruction performance** : 35%-64% of the original SSIM score is preserved when the central region is only considered.

strated here. The conducted experiments highlights the similarities in the characteristics of the regions of our learned filters compared to the theoretical implementations of the GPC filter. Overall, our learned filters show *superior performance* by adjusting the amplitude along with the phase of the transmission coefficients in both regions to reconstruct the background and foreground appropriately.

B.2. Choice of Loss Function

Based on the empirical results, we choose the Reverse Huber Loss [46] over L1 or MSE loss as it produces better reconstruction quality. We follow a similar procedure for setting the δ threshold as in [25] and it was chosen to be 0.95 of the standard deviation of the ground truth image. The Reverse Huber Loss is defined as [46]

$$L_{\delta}(y, f(x)) = \begin{cases} |y - f(x)| & \text{for } |y - f(x)| \leq \delta \\ \frac{(y - f(x))^2 + \delta^2}{2\delta} & \text{otherwise.} \end{cases} \quad (15)$$

B.3. Effect of the Bias Term in the Learned Transformation Loss

As shown in Table S5, it is evident that including a bias term does not introduce a significant improvement in the performance of the network. Since our goal is to develop all-optical systems with minimal/ no post-processing we chose to move forward with a scalar for S and $B = 0$ for \mathcal{L}_{LT} loss.

C. Dataset description

C.1. Phase MNIST digits

Similar to the MNIST digit dataset, the Phase MNIST dataset contains 60000 samples, where we utilize 50000, 5000, 5000 images respectively, for training, validation, and testing methods.

Method	Performance (SSIM \uparrow)	
	WB	WoB
LFF+ GPC init + \mathcal{L}_{LT}		
MNIST	0.9302	0.9184
HeLa	0.5748	0.5719
Bacteria $[0, 2\pi]$	0.9767	0.9820
PhaseD2NN+ \mathcal{L}_{LT}		
MNIST	0.9308	0.9146
HeLa $[0, \pi]$	0.6544	0.6254
HeLa $[0, 2\pi]$	0.4782	0.4654
Bacteria $[0, 2\pi]$	0.9800	0.9915

Table S5. Performance evaluation of the learnable Fourier filter and PhaseD2NN on different datasets when the learned transformation loss is used with a scalar S with (WB) and without (WoB) bias term B .

C.2. HeLa Dataset

Total of 10344 examples with complex fields of HeLa cells are divided to 80%, 10%, 10% for training, validating, and testing of the methods. The electric field amplitudes are normalized to $[0, 1]$ based on the maximum amplitude obtained through the steps described in Section C.2.2. To remove outliers in the phase, values are clipped to $[0, 2\pi]$.

Furthermore, to study the effect of the distribution of phase values in a limited range, the phase information of the above dataset is re-scaled to $[0, \pi]$ and considered as another dataset for reporting performance.

C.2.1 Sample Preparation:

HeLa cells were grown in a standard humidified incubator at 37 °C with 5% CO2 in minimum essential medium supplemented with 1% penicillin/streptomycin and 10% fetal bovine serum. Cells were seeded into the Polydimethylsiloxane chamber of 10 mm \times 10 mm size with 150 μ m thickness on a reflecting silicon substrate. The cells were left in the incubator for 1-2 days for their growth in a densely packed manner and fixed for \sim 20 min using 4% paraformaldehyde in phosphate buffered saline. The sample is then sealed with # 1.5 cover glass from the top which enabled to use water immersion objective lens for imaging and also avoided any air current in the specimen.

C.2.2 Quantitative Phase Imaging:

For quantitative phase imaging, HeLa sample is placed under the Linnik interferometer based quantitative phase microscopy (QPM), which works on the reflection mode. The sample is illuminated with partially spatial and highly temporal coherent light source also called pseudo-thermal light source to generate high quality interferometric images. This

light source illumination has unique advantages such as high spatial and temporal resolution, high spatial phase sensitivity, extended range of optical path difference adjustment between the interferometric arms etc over conventional light sources, e.g., lasers, white light, and light emitting diodes [1]. More details of the experimental setup can be found in previous work [1]. The imaging of HeLa cells is performed using high resolution water immersion objective lens (60×/1.2NA) at 660 nm wavelength. This provided the theoretical transverse resolution approximately equal to 275 nm, which is quite good for high resolution phase recovery of the specimens. The interferometric data is recorded with 5.3 Megapixels ORCA-Fusion digital CMOS camera (model # C14440-20UP). The camera sensor has 2304 × 2304 pixels with 6.5 μm pixel size and provided fairly big 225 μm x 225 μm FOV at 60× optical magnification in QPM system. We acquired approximately 500 such FOVs of different region of interests of the HeLa sample and each FOV contained roughly 50 – 60 cells. The recorded interferometric images are further post processed with random phase-shifting algorithm based on principal component analysis [38] for the recovery of the complex fields related to HeLa cells.

C.3. Phase Noise Dataset

We created different phase noise datasets for two sparsity levels for the evaluation of the generalizability of PhaseD2NN as explained in Section 4.3 of the main text. These datasets are named *Sparse noise dataset* and *Dense noise dataset*. The amplitude of the noise images are set to unity while the phase (ϕ_{in}^{noise}) is sampled from standard normal distribution.

Algorithm 1 shows the procedure to generate noise datasets for different sparsity levels. p_{thresh} is the noise sparsity level. We set $p_{thresh} = 0.1$ and $p_{thresh} = 0.9$ for the sparse and dense noise datasets respectively. Furthermore, to cover a wide range of sparsity levels we generated a third dataset called the *Wide noise dataset* with a similar phase and amplitude setup, however with p_{thresh} set to values within the range [0.1, 1.0] with increments of 0.1.

Algorithm 1 Generating noise dataset with different sparsity levels

```

for  $\phi(x, y)$  in  $\phi_{in}^{noise}$  do
  if  $\phi(x, y) \geq p_{thresh}$  then
     $\phi(x, y) = 0$ 
  end if
end for

```

D. Further Experiments

D.1. Towards Generalized Learnable Phase Retrieval

To analyze the ability of our framework to learn a generalized filter, we train the model on 3 different noise datasets namely: 1. Wide Noise, 2. Sparse Noise, 3. Dense Noise datasets that have different noise levels (refer to section 5.1).

We considered training the proposed model on the noise dataset in two ways: 1. Train to reconstruct the input phase at its output intensity, 2. Train to reconstruct the input phase at its output amplitude. The resultant models are evaluated on phase to intensity conversion task with MNIST and HeLa $[0, \pi]$ (Table S6).

The model trained on the wide noise dataset for phase to intensity conversion (A) shows similar performance on both datasets, while the same experiment but trained for phase to amplitude (B) shows worse performance on both datasets. This indicates that the model trained on phase to amplitude reconstruction with the wide noise dataset surprisingly has better generalizability on phase to intensity reconstruction task on both MNIST and HeLa datasets.

We conduct similar experiments with the sparse and dense noise datasets as well. We observe that the models trained with sparse noise dataset perform (C, D) well with the MNIST dataset while the models trained with dense noise dataset (E, F) perform well with the HeLa dataset. This shows that MNIST, HeLa datasets have similar sparsity-related characteristics compared to sparse, dense noise datasets respectively. This further shows that our model is generalizable among the datasets which have similar sparsity properties as the training dataset.

Dataset	Performance (SSIM \uparrow)	
	MNIST	HeLa $[0, \pi]$
A) Wide noise*	0.3898	0.3728
B) Wide noise [†]	0.2536	0.3585
C) Sparse noise*	0.5743	0.0698
D) Sparse noise [†]	0.7774	0.1184
E) Dense noise*	0.1731	0.3943
F) Dense noise [†]	-0.3694	0.1432

* Noise dataset trained for phase-to-amplitude reconstruction

[†] Noise dataset trained for phase-to-intensity reconstruction

Table S6. Performance evaluation of the learnable Fourier filter on MNIST and HeLa datasets after training on noise datasets.